Numerical and experimental analysis of labyrinth seals with rhomboidal cells

applied sciences

MDPI

Article

Numerical and Experimental Analysis of Labyrinth Seals with Rhomboidal Cells

Elena Campagnoli *, Alessio Desando, Maria Pia Monterossi and Andrea Rapisarda

Department of Energy, Politecnico di Torino, C.so Duca degli Abruzzi 24, 10129 Torino, Italy; alessio.desando@polito.it (A.D.); mariapia.monterossi@polito.it (M.P.M.); andrea.rapisarda@polito.it (A.R.)
* Correspondence: elena.campagnoli@polito.it; Tel.: +39-011-0904506

Abstract: The labyrinth seals are devices commonly used in turbomachinery to reduce hot gas leakages through engine clearances, which adversely affect the gas turbine performance. For this reason, in the last decades, many in-depth analyses and optimization studies were carried out on this topic using experimental, analytical and numerical approaches. In this work, an innovative rhomboidal pattern is presented, obtained through Computational Fluid Dynamics (CFD) simulations, which is more dissipative than commonly used honeycomb cells. The experiments, performed using a Test Article that reproduces a stage and the next stator of a real low-pressure turbine suitably scaled, allowed to validate the numerical results in a situation that closely approximates the real one of use. The results obtained show that the leakages flow fraction of the total mass flow rate that bypasses the blade, which is 29.4% using a honeycomb pattern, is reduced to 27% with rhomboidal cells. The experimental results also made it possible to verify that the new pattern also behaves well from a thermal point of view, giving rise to temperature differences with respect to the honeycomb of less than 1%.

Keywords: labyrinth seal; rhomboidal cell; low-pressure turbine

Citation: Campagnoli, E.; Desando, A.; Monterossi, M.P.; Rapisarda, A. Numerical and Experimental Analysis of Labyrinth Seals with Rhomboidal Cells. *Appl. Sci.* **2021**, *11*, 1371. https://doi.org/10.3390/app11041371

Received: 12 January 2021
Accepted: 28 January 2021
Published: 3 February 2021

1. Introduction

Decreasing the leakage flow in turbomachinery is one of the goals researchers have tried to achieve in the last decades in order to improve efficiency. With this aim, many different studies have been carried out to enhance the effect of the sealing systems, applied to partially prevent flow losses through the unavoidable gaps between the static and rotating parts.

Different typologies of labyrinth seals, lots of which are made of abradable materials, have been both numerically analyzed and experimentally tested: Straight–through, stepped, and staggered labyrinth seals, coupled with different tooth geometries (standard teeth, rounded-edge teeth, slanted teeth, etc.).

Regardless of the chosen configuration, the efforts have been mainly devoted to understanding how the different parts (abradable land and teeth) contribute to the dissipation of the kinetic energy of the flow. For this reason, and in order to perform an optimization of the shape that allows reducing the discharge coefficient, the behavior of the flow along these tortuous paths has been studied through an in-depth characterization of both the flow separation mechanisms and the different recirculation phenomena.

Several authors investigated the flow features in labyrinth seals using both numerical and experimental methods [1–6].

Schramm et al. [7] reported the numerical and experimental analyses carried out to examine the flow patterns through honeycomb lands. Kim et al. [8] performed numerical analyses on straight and stepped seals, evaluating both the discharge coefficient at different clearances and pressure ratios and the dissipative effects produced thanks to the vortices that occur in the sealing cavities.

Chougule et al. [9], based on parametric studies performed on tooth height and thickness and on cell shape, proposed an innovative low leakage labyrinth seal with staggered honeycomb cells.

Recently Čižek et al. [10] showed, through Computational Fluid Dynamics (CFD) simulations, that the radial clearance affects the sealing effect in labyrinth seals to a greater extent than positioning the teeth on the stator or the rotor.

The literature also reports thermal analyses on labyrinth seals, even if, compared to the large amount of fluid dynamic studies, and despite the importance of leakages in determining the thermal behavior of turbomachinery, only a small number of papers deal with the thermal aspects [11–13].

Waschka et al. [11] analyzed, for labyrinth seals, the effects of rotation on the heat transfer coefficients, highlighting that the highest values are recorded near the tips of the teeth and inside the cells, on the wall facing the stator shroud.

Weinberger et al. [12] performed CFD simulations on stepped labyrinth seals, with honeycomb, in order to evaluate the effects of cell geometry and clearance variations on stator temperature.

Micio et al. [13] carried out experimental tests on smooth labyrinth seals to analyze the influence of the Reynolds number on the Nusselt number.

Although many different solutions have been highlighted over the years, research on this topic continues to be of great interest, also due to the new construction techniques recently developed (e.g., direct metal laser sintering). In fact, although the impact of these losses on overall efficiency is very small, considering that modern gas turbines can generate power in the order of megawatts, any improvement in efficiency becomes cost-effective.

In this paper, a previously validated CFD methodology [14] was used to point out a configuration, alternative to honeycomb cells, capable of guaranteeing a reduction in leakage flow. Several configurations, partly similar to those reported in [15,16], were examined, and among these, the rhomboid pattern, previously proposed in the literature by Tuffs et al. [17], has proved to be the most promising. Subsequently, in order to verify the flow split obtained using the CFD model and to predict the thermal behavior of the new seal, in a more realistic environment, the selected configuration was introduced in the numerical models reproducing the fluid and thermal behavior of the available testing facility (i.e., Thermalcase rig) [18]. Finally, the new type of seal, made using the Direct Metal Laser Sintering (DMLS) technique, was mounted in the Test Article (TA) of the experimental rig. The experimental results allowed validating the numerical predictions about the onset in rhomboidal cells of more dissipative vortices than those generated using the honeycomb for sealing. Thanks to these vortices, the rhomboidal pattern behaves better than the honeycomb one from the fluid-dynamic point of view, while it does not significantly affect the thermal distribution compared to the honeycomb.

2. Numerical Analysis

2.1. CFD Analysis on Schramm Geometry

In order to investigate the leakage behavior of the labyrinth seal, a set of CFD simulations were performed. The present study was carried out on the basis of previous research, accomplished by validating a numerical model [19] on the literature data [7,20]. The reference model is a three-fin stepped labyrinth seal. In this seal, the effects observed on the leakage flow are not only related to the type of cell used in the stator design but also strongly depend on the forward or backward stepped labyrinth seal configuration [21]. The already-validated numerical procedure was applied to a different stator land pattern, composed of rhomboidal cells and the obtained results were compared with the traditional honeycomb cells.

The numerical model was implemented with the software Ansys® CFX 14.5®. This code uses a coupled solver with an algebraic multi-grid approach and a combined algorithm of finite volume and element. The model geometry is shown in Figure 1 and described in Table 1.

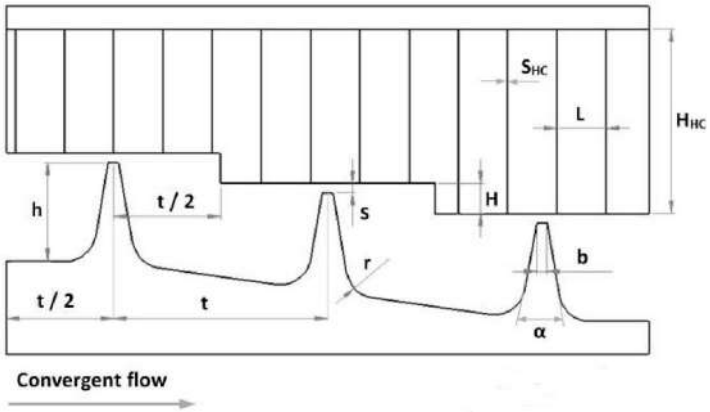

Figure 1. Schramm Model geometry [19].

Table 1. Labyrinth seal geometrical parameters.

Parameter	Description	Value
t	Tooth pitch	28 mm
s	Seal clearance	1.204 mm
NT	Number of teeth	3
H	Step height	3.92 mm
h	Tooth height	12.88 mm
b	Fin tip thickness	1.316 mm
r	Fin tip fillet	4 mm
α	Angle between tooth faces	20 deg

In addition to the honeycomb land (whose geometrical parameters are listed in Table 2 and illustrated in Figure 2), rhomboidal cells were analyzed as an alternative pattern. Three kinds of cells were obtained by changing the diagonal ratio, which is defined in Equation (1).

$$C_R = \frac{D_M}{D_m} = \frac{1}{tan\delta}\,, \tag{1}$$

Table 2. Honeycomb cell geometrical parameters.

Parameter	Description	Value
L	Diameter	3.22 mm
H_{HC}	Depth	24.08 mm
S_{HC}	Cell wall thickness	0.07 mm

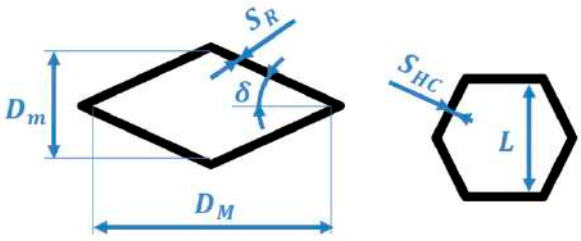

Figure 2. Rhombus (**left**) and honeycomb (**right**) cells.

The design constraint imposed for the rhombi is to keep their minor diagonal, which is disposed in the flow direction, equal to the honeycomb cell diameter.

The investigation of the rhomboidal pattern consisted of a CFD numerical sensitivity, performed by modifying the ratio of the diagonals to point out the effects on the leakage flow

of the labyrinth seal. The names of the different generated patterns, with their respective C_R, δ, and cell area ratio (with respect to the honeycomb cell) are listed in Table 3.

Table 3. Rhomboidal pattern design: rhombus diagonal ratio C_R, half of rhombus minor angle δ, ratio between the area of the rhomboid cell (A_R) and that of the honeycomb (A_{HC}).

Pattern	C_R (-)	δ (-)	A_R/A_{HC} (-)
R1	2	26.6	1.155
R2	3	18.4	1.732
R3	4	14.0	2.309

The CFD model used is static and isothermal. While Schramm [7] dealt with turbulence using the k-ε model, paying special attention in setting y+ near the wall domain, in this paper, instead, the two-equation model k-ω with automatic wall treatment was chosen, referring to the previous analyses performed by Yan [21]. The reason for this choice is that this model proved to perform better with adverse pressure gradients or separating flows as it accurately replicates the vortex pattern that is generated in the sealing cavity [22]. The computational domain has a width of two cells, with the condition of translational periodicity applied to the lateral boundaries (Figure 3). The outlet duct has an opening boundary condition in order to allow recirculating flows during the simulations. The stator cells above the tip of the first fin are centered on the fin tip. The setup settings are shown in Table 4.

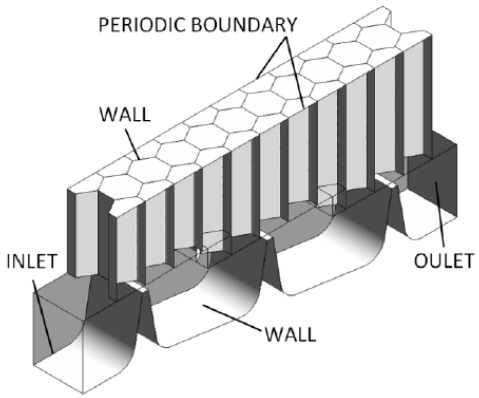

Figure 3. CFD geometry, boundary conditions [19].

Table 4. Setup settings.

Outlet static pressure	p_0 = 1.01325 bar
Pressure ratio	1.1
Total inlet temperature	T_0 = 300 K (Isothermal)
Solution scheme	Upwind–First Order
Turbulence model	k-ω
Y+	Automatic wall treatment
Analysis	Steady state
Fluid	Air ideal gas (Sutherland)
Turbulence intensity	5%

The mesh is composed of hexahedrons. The number of nodes for each simulation is shown in Table 5, while Figure 4 shows the detail of the grid of the rhomboidal cell. In the CFD model, the fin tip region and the stator land are connected by means of the General Grid Interface (GGI) scheme, which is suitable when the analyzed model is

composed of multiple bodies having non-conformal grids at the interface. The pressure ratio is calculated between the inlet total pressure and the static outlet pressure. The calculations were performed with a Dell Precision T7600 computer, with two Intel Xeon CPU E5-2620 processors.

Table 5. Mesh details for the Honeycomb cell (HC) and for the three rhomboidal cells (R1, R2, R3).

Pattern	# Nodes
HC	600,000
R1	780,000
R2	1,225,000
R3	1,700,000

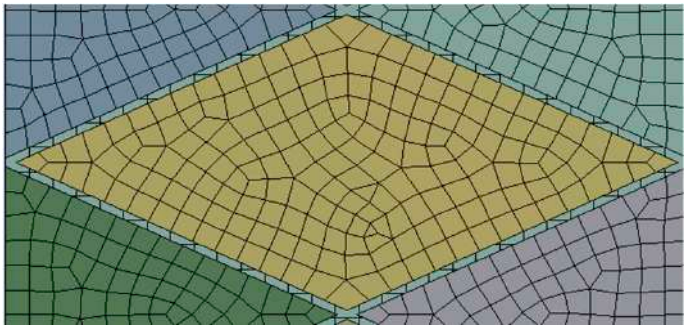

Figure 4. Mesh rhomboidal cell detail.

Since each model has a different lateral width, comparing the numerical values of the leakage mass flow rates is not possible. In the present work, the discharge coefficient will be used to compare the performance of the several patterns analyzed:

$$C_D = \frac{\dot{m}_{CFD}}{\dot{m}_{ideal}}, \tag{2}$$

where $\dot{m}_{CFD}$ is the mass flow rate recorded during the numerical simulations, while $\dot{m}_{ideal}$ is obtained with the following formula, proposed by Martin [23]:

$$\dot{m}_{ideal} = \frac{p_0 \times A}{\sqrt{T_0}} \sqrt{\frac{2\kappa}{R(\kappa-1)} \left[\left(\frac{1}{\beta}\right)^{2/\kappa} - \left(\frac{1}{\beta}\right)^{(\kappa+1)/\kappa} \right]}, \tag{3}$$

Air (ideal gas) was used in the numerical model, meaning that R = 287 J/kgK and κ = 1.4.

Area A in Equation (3) is based on the nominal clearance value. Here, an important observation has to be made before showing the CFD results. When a pattern is utilized for the abradable stator land, the effective gap that can be measured between the fin tip and the closest cell wall can be significantly greater than the nominal clearance value s. In particular, a local value of effective clearance s_{eff} (y) can be defined. This value depends on the cell-fin tip misalignment d and on the function $q(y)$, which represents the contour of the cell in the tangential direction [19]:

$$s_{eff} = \sqrt{s^2 + \left(q(y) - d - \frac{b}{2}\right)^2}, \tag{4}$$

where d has been set equal to zero, while $q(y)$ is a periodical function defined by intervals. Figure 5 shows the points used in Equation (5) below:

$$\begin{array}{c} from\ A\ to\ B\ q(y) = 0 \\ from\ B\ to\ C\ q\ (y) = \left(y - \frac{S_R}{2}\frac{1}{\sin\delta}\right) \times \sin\delta \\ from\ C\ to\ D\ q(y) = (D_m - b)/2 - \left(y - \left(\frac{D_M}{2} + \frac{S_R}{2}\frac{1}{\sin\delta}\right)\right) \times \sin\delta \\ from\ D\ to\ E\ \times\ q(y) = 0 \end{array} \quad (5)$$

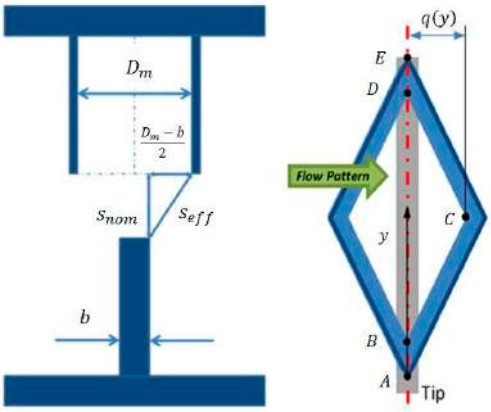

Figure 5. Nominal and effective clearance.

By applying the procedure described above for the honeycomb cells [19] to Equations (4) and (5), it is possible to calculate the clearance values s_{mean} and s_{seal}. The first represents the local average clearance value and refers to the single tooth, while the second is the average value among all the teeth of the labyrinth seal.

Zimmermann et al. [20] took into account, for the first time, the contribution to leakage flow, due to the difference between effective and nominal clearance, introducing a geometrical increase parameter ζ_g for honeycomb labyrinth seals. *A* similar definition, based on the averaged clearance s_{seal}, is proposed in the present work:

$$\zeta_g = \frac{s_{seal}}{s}\,, \quad (6)$$

The leakage mass flow rates, recorded in the numerical simulations, are used to calculate the discharge coefficients shown in Figure 6. Table 6 reports the percentage variation calculated with the formula reported in Equation (7) and using the smooth labyrinth seal as a reference value.

$$\Delta C_D\% = \frac{C_{D,x} - C_{D,\,Smooth}}{C_{D,\,x}} \times 100\,, \quad (7)$$

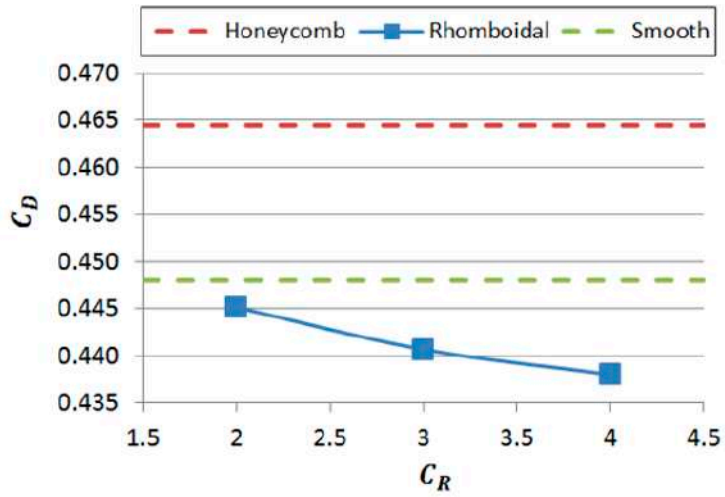

Figure 6. Discharge coefficient for the analyzed patterns.

Table 6. C_d percentage variation.

ΔC_d % (Reference = Smooth)	
HC	+3.68
R1	−0.64
R2	−1.64
R3	−2.23

As known from the literature [20], stepped honeycomb labyrinth seals generally exhibit greater leakage flows than the equivalent smooth seal, when the cell diameter is larger than the clearance. The advantages of using the honeycomb pattern is mostly related to a lower density of the abradable material and better convective heat transfer within the cells [24]. The rhomboidal cells not only have these advantages, but also promote a stronger dissipation, leading to a leakage flow, which is even lower than the smooth seal. Moreover, this mechanism resulted in being more effective when rhombi with higher diagonal ratios were simulated.

The reduction of the discharge coefficient for rhomboidal cells can be explained considering two different contributions. The first one is related to the shape of the cells that, unlike honeycomb cells, do not have edges perpendicular to the direction of flow. The absence of these perpendicular edges acts on the carry-over, promoting strong axial and vertical velocity gradients. Consequently, complex vorticous structures arise in the downstream cavity which are more dissipative not only than in the honeycomb cells, where this phenomenon occurs to a limited extent, but also than in smooth labyrinth seals.

The second effect can be explained with a more detailed analysis of the geometrical increase parameter, shown in Figure 7. All the analyzed patterns exhibit a geometrical increase parameter approaching the value ζ_g = 1 (i.e., the smooth configuration). In particular, the averaged seal clearance calculated for the rhomboidal cells is significantly smaller than the value recorded for the honeycomb labyrinth seal. Moreover, as the diagonal ratio increases, ζ_g slightly decreases.

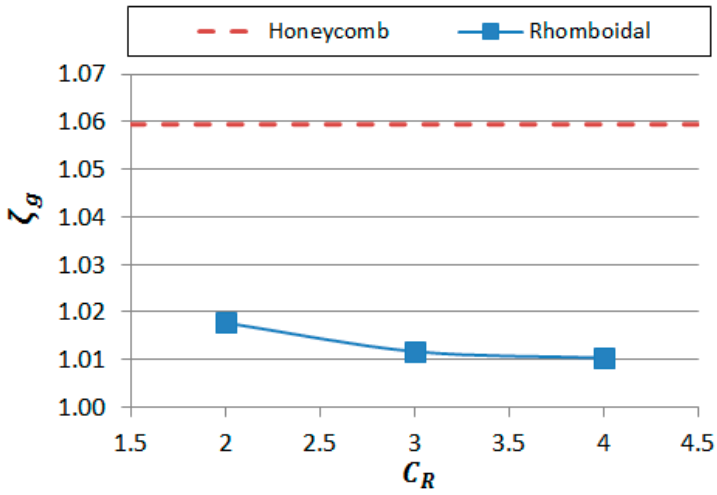

Figure 7. Geometrical increase parameter for the analyzed patterns.

As pointed out by previous studies [19,21], a smooth forward-stepped labyrinth seal shows two cavity counter-rotating vortices, which strongly dissipate the kinetic energy. This phenomenon, clearly visible in the vector velocity plot shown in Figure 8a, is due to the carry-over flowing directly towards the seal step. Here, the airflow impacts the step and is deflected by ninety degrees. The presence of any empty cell in the same typology of labyrinth seal may change this vorticous structure. When $\zeta_g \gg 1$ the carry-over is already deflected by the cell wall. Although the interaction between cell wall and carry-over generates friction, which partially dissipates its kinetic energy, the flow deflection is enough to avoid the impact on the seal step. Consequently, the cavity vortices show a different structure. The condition $\zeta_g \approx 1$ indicates that the effective seal clearance is practically equal to the nominal value. In this case, the structures observed in the seal cavities should be similar to those occurring in the smooth labyrinth seals. Indeed, the labyrinth seal with the rhomboidal cells shows stronger downstream vortices compared to the honeycomb seal, due to its smaller ζ_g (compare Figure 8b,c). However, the rhomboidal cells are even more dissipative than the smooth configuration, as they add the friction contribution that occurs near the fin tips.

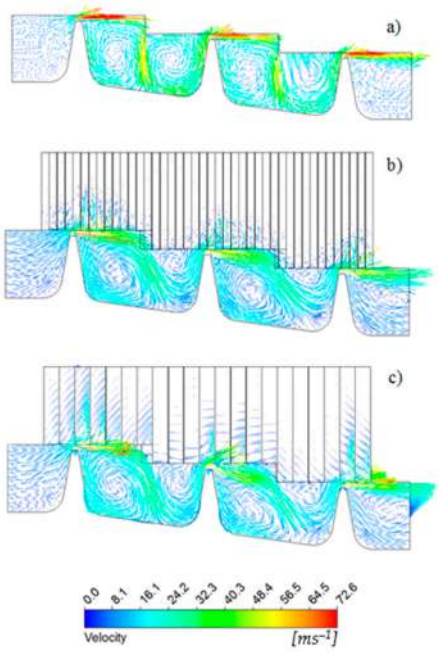

Figure 8. Velocity vector plot for smooth (**a**), honeycomb (**b**), and rhomboidal $C_R = 4$ (**c**).

2.2. CFD Analysis on Test Article Geometry

As described in [14,18], the Test Article replicates one stage and the next stator of an aeronautical Low Pressure Turbine (LPT), properly scaled. Within the Test Article (TA) (Figure 9), there are three different mass flow rates. Two of the three mass flow rates stream into the lower chamber: the main mass flow, i.e., the Flow Path (FP) and the Cooling (Coo), while the last mass flow rate, the Active Clearance Control, flows into the separate upper chamber.

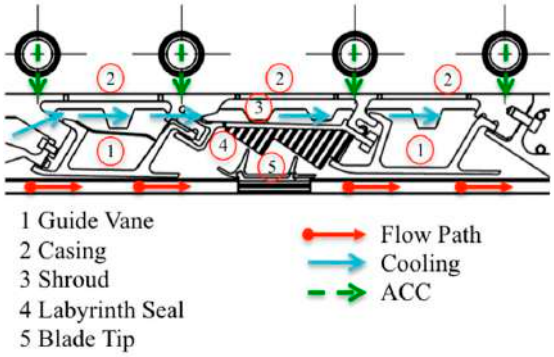

Figure 9. Main components and mass flow rates [14].

Since there are no rotating parts in the TA, the pressure drop dictated by the blade on the FP is reproduced thanks to the introduction of a flow restrictor below the blade tip. This restrictor (Figure 10) was designed to obtain a fixed pressure drop (blade upstream-downstream) $\beta = 1.1$.

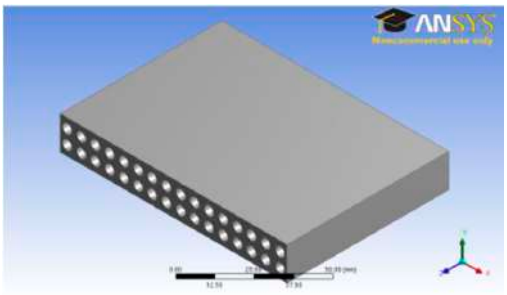

Figure 10. Flow restrictor [14].

The area of the TA (Figure 9) in which the restrictor, the tip of the blade and, in front, the labyrinth seal are positioned is the one considered to perform the CFD analysis on the TA geometry.

The CFD analysis was carried out reproducing the rhomboidal pattern R3 (see Table 3), which shows the greatest reduction in the discharge coefficient in the CFD model. For the numerical simulations, only the FP was considered because it is only on this mass flow rate that the labyrinth seal acts to minimize leakages.

The aim of this analysis is to use the validated numerical models to predict the leakage behavior of this alternative pattern. Figure 11 shows the boundary conditions, while for the setup settings, we can refer to Table 4, except for the total inlet temperature.

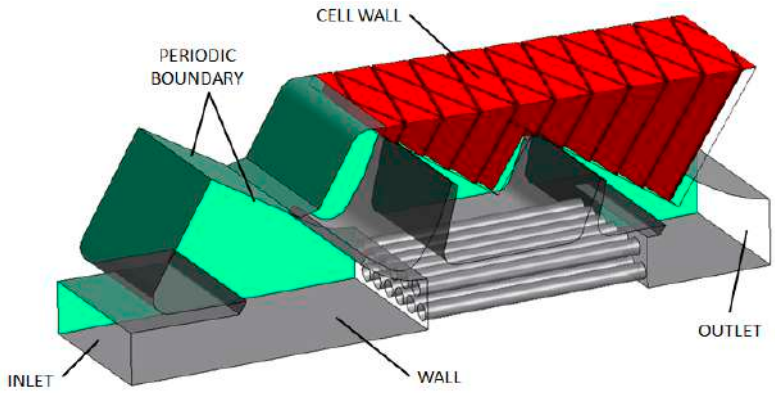

Figure 11. Test Article (TA), boundary conditions.

The inlet temperature to perform the CFD simulation has been set at 873 K, as this temperature is the maximum temperature to which the FP can be heated. The pressure drop β, due to the rotating blade, was set equal to 1.1 in accordance with what happens in the TA.

Figure 12 represents the area under the labyrinth seal and reports the three mass flow rates of interest. In Figure 12, $\dot{m}_{FP}$ is the total FP mass flow rate, while $\dot{m}_{restr}$ and $\dot{m}_{leak}$ are the mass flow rates flowing through the restrictor and labyrinth seal, respectively.

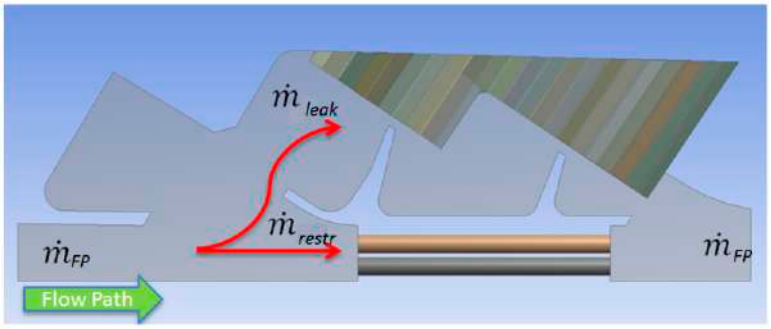

Figure 12. Mass flow split for the CFD model.

Both $\dot{m}_{FP}$ and $\dot{m}_{restr}$ were calculated in the CFD model. The first one is calculated at the inlet of the CFD domain and the second at the inlet of the flow restrictor holes. The leakage flow rate $\dot{m}_{leak}$ was calculated by subtraction. The simulation performed shows that 73% of the mass flow rate passes through the restrictor, while the remaining 27% flows above the fin tip. This leakage flow is lower than the one previously calculated [14] using honeycomb cells, which was equal to 29.4%. This result is in agreement with the results reported in the previous paragraph, obtained by performing the CFD analyses on the test model.

2.3. Thermalcase Models Predictions

The third phase of the numerical analysis was performed using the two numerical models representing the phenomena taking place within the TA used to carry out the experiments (Figure 13). These two models are used, one for fluid network analysis (Flowmaster) and the second for thermal analysis (Patran/P-Thermal). The fluid network is reproduced in Patran/P-Thermal using 1D element with two nodes (advection bars). Using this method and simply assigning the airflow and direction to each of the bars in the network, it is possible to reproduce in the P-Thermal model the elements used in Flowmaster. During the calculation, the mass flow rates and the temperatures information are shared between the two models until the fluid and thermal balance is reached.

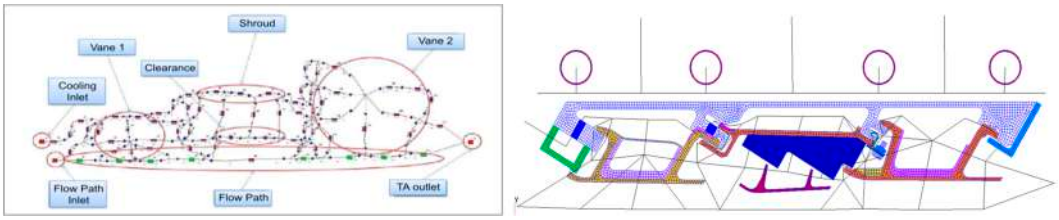

Figure 13. Fluid network (**left**) and thermal network (**right**).

The two described numerical models allow reproducing the fluid dynamic and thermal fields inside the TA. For this reason, these models can be used to further investigate the impact of rhomboidal cells and, in particular, to verify the reduction of the leakage flow and to predict the impact of the new seal on the temperature distribution in the surrounding area.

Initially, some adjustments to the fluid network and to the 2D thermal model described in [25,26] were necessary to adequately model the innovative cell features. In particular, in the fluid network, the elements representing the honeycomb cells were replaced with rhombi.

The purpose of this third numerical investigation is to provide an overview that is representative of the real operating conditions. For this reason, the numerical model includes all the typical mass flow rates that can be observed within an AGTE (Aircraft Gas Turbine Engine) and which are also modeled within the TA, unlike the CFD simulations that model only the FP mass flow rate. In standard operating conditions, two other flows are active within the TA with engine thermal control functions [18]. The first one is the Cooling mass flow rate (Coo), which flows in the casing upper cavities and prevents hot gas ingestion through the gaps among the different components. The second one is the Active Clearance Control (ACC) mass flow rate used, as well known, to control the clearance height during the different flight phases.

A first part of the analysis was performed simply using the fluid network and considering only the mass flow rates of FP and Coo because, as explained in [14], the ACC stream, which flows in a separate channel, does not interact with the other two flows from the fluid dynamic point of view. Two numerical simulations were performed by setting the temperature of the FP equal to 873 K and $\beta = 1.1$. To highlight the possible presence of effects on the split of the FP between the restrictor and the tip of the fin, due to the temperature of the Coo, in the simulations, two different Coo temperatures are used. Table 7 shows the used set-up values and the resulting FP split, which allows us to state that the Coo temperature does not significantly influence the behavior of the labyrinth seal. Figure 14, which reproduces the zone in which the restrictor, the blade tip, and the labyrinth seal are positioned, shows the split of mass flow rates obtained numerically for the two examined cases.

Table 7. Set up values and Flow Path (FP) mass flow rate split.

Case	T_{FP} (K)	β (-)	T_{Coo} (K)	$\dot{m}_{restr}$ (%)	$\dot{m}_{leak}$ (%)
A	873	1.1	473	72.8	27.5
B	873	1.1	573	72.9	27.4

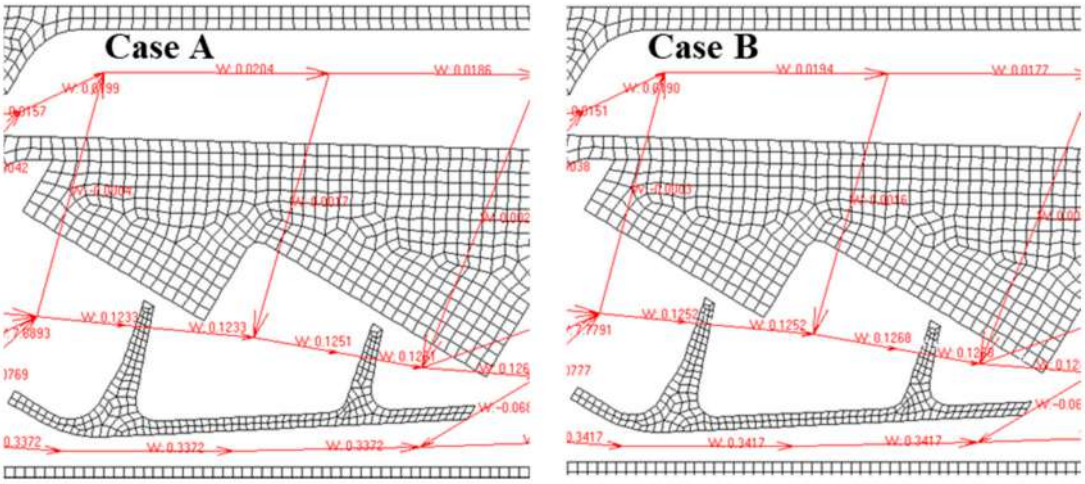

Figure 14. Thermalcase model: Mass flow split in the sealing region with a Flow Path temperature of 873 K and a Cooling temperature in Case A (**left**) of 473 K and in Case B (**right**) of 573 K.

The results obtained with the Thermalcase fluid network are in good agreement with those provided by the CFD analyses. As can be seen, in Table 7, the sum of the two percentage fractions of the total mass flow rate, which flow respectively inside the restrictor and in the clearance, slightly exceed 100%. This is because the mass flow $\dot{m}_{leak}$ that bypasses the fin of the tip (Figure 12) includes a small amount of Coo air coming from the upper cavities.

Changes were also made to the thermal model before performing the coupled fluid thermal analysis. These changes were necessary to take into account the effect of the new cell geometry on thermal conductivity and thus on heat transfer in the labyrinth seal region. The change of thermal conductivity does not represent a real variation of the thermo-physical properties since the material and the operating temperature range are the same used to test the honeycomb cell, but it is necessary to take into account the different solid/void ratio.

Since only the solid parts of the cells contribute to conduction heat transfer, the scale factor reported in Equation (8) was applied to the thermal conductivity of the rhomboidal cell.

$$f_{scale} = \frac{A_s}{A_s + A_v}, \tag{8}$$

However, due to the chosen cell thickness and solid/void ratio, the conductivity scale factor is quite similar to the honeycomb one, producing only a negligible effect on the heat transfer by conduction. For the convective heat transfer, the exchange coefficients were modified since, at the same height, the area of the rhomboidal cell is greater than the honeycomb one, and therefore, the portion of the shroud back-plate to be considered for the convective heat transfer is greater.

After these modifications, two numerical simulations were carried out to examine the thermal behavior of the new seal. The settings used (Table 8) refer to two experimental tests (Test 3 and Test 4 [14]) previously used for tuning the numerical model with the honeycomb seal.

Table 8. Settings for the numerical simulations: temperatures, pressure and mass flow rates for the Flow Path, Cooling and Active Clearance Control.

Test	T_{FP} (K)	p_{FP} (bar)	$\dot{m}_{FP}$ (kg/S)	T_{Coo} (K)	p_{Coo} (bar)	$\dot{m}_{Coo}$ (kg/s)	T_{ACC} (K)	p_{FP} (bar)	$\dot{m}_{ACC}$ (kg/s)
3	796	1.8	0.438	461	2	0.043	329	1.04	0.013
4	808	1.8	0.442	569	2	0.044	336	1.05	0.013

In analyzing the results, particular attention was paid to three metal (M#) and one air (T#) thermocouples (Figure 15) placed in the area of interest.

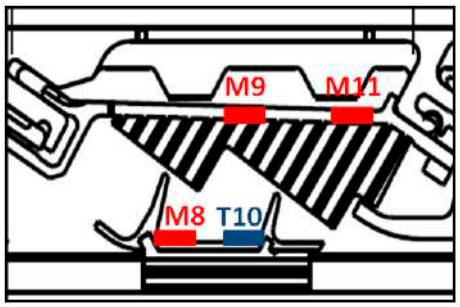

Figure 15. Thermocouples placed in the seal region.

In Tables 9 and 10, the temperatures resulting from the numerical simulations with the rhomboidal cells are compared with the numerical data previously obtained with the honeycomb cells [14].

Table 9. Test 3: Numerical temperature of honeycomb and rhomboidal cells.

Temperature (K)	M9	M11	M8	T10
$T_{HC,num}$	702.8	674.4	772.7	758.5
$T_{RB3,num}$	696.3	668	771.2	752.8
ΔT	−6.5	−6.4	−1.5	−5.7

Table 10. Test 4: Numerical temperature of honeycomb and rhomboidal cells.

Temperature (K)	M9	M11	M8	T10
$T_{HC,num}$	729	705.2	786.2	772.8
$T_{RB3,num}$	722.9	699.5	784.4	767
ΔT	−6.1	−5.9	−1.8	−5.8

It is possible to observe that the numerical temperatures obtained with the rhombi are only slightly lower than those recorded for the honeycomb and that this temperature difference can be considered negligible when compared with the high operating temperatures.

3. Experimental Results

After installing the new seal (Figure 16) in the TA, the experiments were performed by adjusting the temperatures, pressures, and mass flow rates to reproduce the same conditions under which the honeycomb cell had been experimentally tested (Table 8).

Figure 16. Test Article (TA) stator land with R3 rhomboidal cells.

The conditions at the different TA inlets for the rhomboidal cells are shown in Table 11. It is possible to note that only the Active Clearance Control (ACC) temperatures differ

from those previously used. This is because the ACC supply line is not equipped with an electrical heater, and therefore, the ACC temperature is not regulated, but it is simply measured [18].

Table 11. Experimental inlet conditions for the rhomboidal cells.

Test	T_{FP} (K)	p_{FP} (bar)	$\dot{m}_{FP}$ (kg/s)	T_{Coo} (K)	p_{Coo} (bar)	$\dot{m}_{Coo}$ (kg/s)	T_{ACC} (K)	p_{FP} (bar)	$\dot{m}_{ACC}$ (kg/s)
3 bis	797	1.8	0.437	460	2	0.043	314	1.06	0.013
4 bis	807	1.8	0.441	567	2	0.044	321	1.05	0.013

For this reason, to evaluate the impact due to lower ACC temperatures, especially in the shroud region (thermocouples M9 and M11), two numerical simulations were performed using the input conditions reported in Table 10.

The exam of the numerical results revealed a more than limited effect in the shroud region, with a decrease of the temperature of about $1 \div 1.5$ K, which authorizes the comparison between the experimental results obtained with rhomboidal and honeycomb cells.

Tables 12 and 13 compare the temperatures in the sealing region (see Figure 15) obtained using the two different types of cells.

Table 12. Temperature in the labyrinth seal region for test 3 and test 3 bis.

Temperature	Shroud		Fin Tip	
(K)	M9	M11	M8	T10
$T_{HC,exp}$	728.5	693.3	782.7	751.0
$T_{RB3,exp}$	723.1	691.1	780.5	754.2
ΔT	−5.4	−2.8	−2.2	+3.2

Table 13. Temperature in the labyrinth seal region for test 4 and test 4 bis.

Temperature	Shroud		Fin tip	
(K)	M9	M11	M8	T10
$T_{HC,exp}$	751.7	725.6	797.3	774.5
$T_{RB3,exp}$	749.1	722.0	795.2	774.2
ΔT	−2.9	−3.6	−2.1	−0.3

The experimental results show that by using the rhomboidal cells, a decrease of the temperature in the region of the labyrinth seal of about $3 \div 5$ K is obtained, which confirms the numerical forecast. If we compare this decrease with the mean temperature recorded in this region, the percentage reduction obtained is less than 1%. This observation allows us to conclude that while the new seal shows a positive effect in reducing the leakage flow, its impact from the thermal point of view is negligible.

4. Discussion and Conclusions

This research presents a detailed analysis of the performance of an innovative labyrinth seal. In particular, three different patterns were proposed, alternative to the standard honeycomb, with a rhomboidal shape. The numerical models developed and validated in a previous study [14] were used to predict the performance of these innovative cells, and experimental tests were performed using the most promising alternative pattern.

The parameter for the design of the rhomboidal cell was the ratio of the diagonals and, using the CFD approach, the three different rhomboidal patterns were evaluated, examining their discharge coefficient. All the cells analyzed turned out to be more dissipative than both the smooth labyrinth seals and the honeycomb ones, while maintaining the same pattern density as the honeycomb cells.

The CFD analyses allowed highlighting that the rhomboidal cells perform better for two reasons. The first one is related to the effective clearance, since the geometrical increase parameter, ζ_g, for all the proposed rhomboidal patterns is around 1. In practical terms, this condition promotes the formation of stronger and, thus, more dissipative vortex structures within the seal cavities. In addition, the interaction between the carry-over and the cell wall near the fin tips introduces a second contribution related to friction, which allows the rhombi to perform even better than the smooth seal.

Furthermore, the CFD analyses revealed that in the examined rhomboidal patterns, this dissipative effect increases with the ratio of the diagonals. The R3 cell is indeed the most efficient, with a 2.2% reduction in the discharge coefficient, compared to the smooth seal.

Using the fluid model that reproduces the fluid dynamic behavior of the available Test Article, these numerical results were verified and confirmed for the R3 cell. The comparison of the leakage flows obtained using the honeycomb cell, and the rhomboidal cell showed that the latter is more efficient and that the fraction of the total mass flow rate that bypasses the blade is reduced by 29.4% (honeycomb) to 27% (rhombi).

Using the coupled fluid-thermal model of the TA, the performances of the rhomboidal cells R3 were also evaluated from the thermal point of view. The obtained results showed that the differences with the hexagonal stator land are negligible, less than 1%. The following experimental tests confirmed the numerical forecast, with a good agreement.

Author Contributions: Conceptualization and methodology, E.C., A.D., M.P.M. and A.R.; CFD analysis, A.D. and A.R.; fluid-thermal coupled analysis, M.P.M.; experimental validation, E.C. and M.P.M.; writing—original draft preparation and editing, E.C. and A.D.; Review, E.C., A.D., M.P.M. and A.R. All authors have read and agreed to the published version of the manuscript.

Funding: This research received no external funding.

Institutional Review Board Statement: Not applicable.

Informed Consent Statement: Not applicable.

Data Availability Statement: Not applicable.

Conflicts of Interest: The authors declare no conflict of interest.

Abbreviations

A	Area (m^2)
ACC	Active Clearance Control
AGTE	Aircraft Gas Turbine Engine
b	Fin tip thickness (mm)
C_D	Discharge coefficient (-)
C_R	Rhombus diagonal ratio (-)
CFD	Computational Fluid Dynamics
Coo	Cooling
D	Rhombus diagonal (mm)
d	Cell-fin tip misalignment (mm)
f_{scale}	Scaling factor to account for the solid area to void ratio (-)
FP	Flow Path
H	Step height (mm)
h	Tooth height (mm)
L	Honeycomb diameter (mm)
LPT	Low Pressure Turbine
M#	Metal thermocouple
$\dot{m}$	Mass flow rate (kg/s)
NT	Number of teeth
p	Pressure (bar)

p_0	Outlet static pressure (bar)
q	Cell contour coordinate (mm)
R	Ideal gas constant (J/kgK)
r	Fin tip fillet (mm)
S	Cell wall thickness (mm)
s	Seal clearance (mm)
T	Temperature (K)
T_0	Total inlet temperature (K)
t	Tooth pitch (mm)
T#	Air thermocouple
TA	Test Article
y	Tangential direction coordinate (mm)
Greek letters	
α	Angle between tooth faces (deg)
B	Pressure ratio (-)
δ	Half of the rhombus minor angle (-)
k	Specific heats ratio (-)
ζ_g	Geometrical increase parameter (-)
ΔT	Temperature difference (K)
Subscripts	
ACC	Active Clearance Control
Coo	Cooling
eff	Effective
ex	Experimental
FP	Flow Path
HC	Honeycomb
Ideal	Isentropic condition
leak	Leakage flow
M	Major
m	Minor
num	Numerical
RB	Rhombus
ref	Reference value
restr	Restrictor
s	Solid
v	Void

References

1. Stocker, H.L. Determination and Improving Labyrinth Seal Performance in Current and Advance High Performance Gas Turbine. In Proceedings of the AGARD CP273 Conference Proceedings, London, UK, 6–7 April 1978; pp. 13/1–13/22.
2. McGreehan, W.F.; Ko, S. Power Dissipation in Smooth and Honeycomb Labyrinth Seals. In Proceedings of the ASME 1989 International Gas Turbine and Aeroengine Congress and Exposition, Toronto, ON, Canada, 4–8 June 1989. [CrossRef]
3. Rhode, D.L.; Ko, S.; Morrison, G.L. Leakage Optimization of Labyrinth Seals Using a Navier-Stokes Code. *Tribol. Trans.* **1994**, *37*, 105–110. [CrossRef]
4. Rhode, D.L.; Ko, S.; Morrison, G.L. Experimental and Numerical Assessment of an Advanced Labyrinth Seal. *Tribol. Trans.* **1994**, *37*, 743–750. [CrossRef]
5. Untaroiu, A.; Goyne, C.P.; Untaroiu, C.; Wood, H.G.; Rockwell, R.; Allaire, P.E. Computational Modeling and Experimental Investigation of Static Straight-Through Labyrinth Seals. In Proceedings of the ASME 2008 International Mechanical Engineering Congress and Exposition, Boston, MA, USA, 31 October–6 November 2008. [CrossRef]
6. Min, S.H.; Soo, I.L.; Seong, W.M.; Tong, S.K.; Jae, S.K.; Dong, H.K.; Young, J.I. Effect of Clearance and Cavity Geometries on Leakage Performance of a Stepped Labyrinth Seal. *Processes* **2020**, *8*, 1496. [CrossRef]
7. Schramm, V.; Willenborg, K.; Kim, S.; Wittig, S. Influence of a Honeycomb Facing on the Flow Through a Stepped Labyrinth Seal. *J. Eng. Gas Turbines Power* **2000**, *124*, 140–146. [CrossRef]
8. Kim, T.S.; Cha, K.S. Comparative analysis of the influence of labyrinth seal configuration on leakage behavior. *J. Mech. Sci. Technol.* **2009**, *23*, 2830–2838. [CrossRef]
9. Chougule, H.H.; Ramerth, D.; Ramachandran, D. Low Leakage Designs for Rotor Teeth and Honeycomb Lands in Labyrinth Seals. In Proceedings of the ASME Turbo Expo 2008: Power for Land, Sea, and Air, Berlin, Germany, 9–13 June 2008. [CrossRef]
10. Čížek, M.; Pátek, Z.; Vampola, T. Aircraft Turbine Engine Labyrinth Seal CFD Sensitivity Analysis. *Appl. Sci.* **2020**, *10*, 6830. [CrossRef]

11. Waschka, W.; Wittig, S.; Kim, S. Influence of High Rotational Speeds on the Heat Transfer and Discharge Coefficients in Labyrinth Seals. *J. Turbomach.* **1992**, *114*, 462–468. [CrossRef]
12. Weinberger, T.; Dullenkopf, K.; Bauer, H.-J. Influence of Honeycomb Facings on the Temperature Distribution of Labyrinth Seals. In Proceedings of the ASME Turbo Expo 2010: Power for Land, Sea, and Air, Glasgow, UK, 14–18 June 2010; Volume 4, pp. 921–930. [CrossRef]
13. Micio, M.; Facchini, B.; Innocenti, L.; Simonetti, F. Experimental Investigation on Leakage Loss and Heat Transfer in a Straight Through Labyrinth Seal. In Proceedings of the ASME 2011 Turbo Expo: Turbine Technical Conference and Exposition, Vancouver, BC, Canada, 6–10 June 2011; Volume 5, pp. 967–979. [CrossRef]
14. Campagnoli, E.; Desando, A. Validation of a CFD Model of a Labyrinth Seal for Low Pressure Turbines Using a Fluid-Thermal Tool Tuned Through Experimental Measurements. *Instrum. Mes. Métrologie* **2019**, *18*, 509–516. [CrossRef]
15. Wróblewski, W.; Frączek, D.; Marugi, K. Leakage reduction by optimisation of the straight–through labyrinth seal with a honeycomb and alternative land configurations. *Int. J. Heat Mass Transf.* **2018**, *126*, 725–739. [CrossRef]
16. Szymański, A.; Wróblewski, W.; Bochon, K.; Majkut, M.; Strozik, M.; Marugi, K. Experimental validation of optimised straight-through labyrinth seals with various land structures. *Int. J. Heat Mass Transf.* **2020**, *158*, 119930. [CrossRef]
17. Tuffs, M.; Shipton, M.H.; Mei, J.; Wu, X.; Shipton, J.M. Abradable Seals. U.S. Patent 2004/0265120A1, 30 December 2004.
18. Campagnoli, E.; Monterossi, M.P. Design of a New Test Rig Facility to Study the Turbine Thermal Behaviour. *Int. J. Mech. Control Levrotto Bella* **2018**, *19*, 51–59.
19. Desando, A.; Rapisarda, A.; Campagnoli, E.; Taurino, R. Numerical Analysis of Honeycomb Labyrinth Seals: Cell Geometry and Fin Tip Thickness Impact on the Discharge Coefficient. In Proceedings of the ASME Turbo Expo 2015: Turbine Technical Conference and Exposition, Montreal, QC, Canada, 15–19 June 2015. [CrossRef]
20. Zimmermann, H.; Wolff, K.H. *Air System Correlations: Part 1—Labyrinth Seals*; ASME Paper 98-GT-206; ASME: New York, NY, USA, 1998. [CrossRef]
21. Yan, X.; Li, J.; Feng, Z. Effects of sealing clearance and stepped geometries on discharge and heat transfer characteristics of stepped labyrinth seals. *Proc. Inst. Mech. Eng. Part A J. Power Energy* **2011**, *225*, 521–538. [CrossRef]
22. Andersson, B.; Andersson, R.; Hakansson, L.; Mortensen, M.; Sudiyo, R.; Van Wachem, B. *Computational Fluid Dynamics for Engineers*; Cambridge University Press (CUP): Cambridge, UK, 2011.
23. Martin, H.M. Labyrinth Packings. *Engineering* **1908**, *85*, 35–38.
24. Willenborg, K.; Schramm, V.; Kim, S.; Wittig, S. Influence of a Honeycomb Facing on the Heat Transfer in a Stepped Labyrinth Sea, ASME. *J. Eng. Gas Turbines Power* **2000**, *124*, 133–139. [CrossRef]
25. Fasanella, S.A. Analisi e Taratura di un Modello Numerico per la Simulazione di Componenti Aeronautici Raffreddati. Master's Thesis, Politecnico di Torino, Torino, Italy, April 2013.
26. Monterossi, M.P.; Campagnoli, E. Numerical Modelling for the Prediction of Aircraft Cooled Components Thermal Behavior. In Proceedings of the International CAE Conference, Verona, Italy, 19–20 October 2020.